INORGANIC CHEMISTRY FRONTIERS

RESEARCH ARTICLE

View Article Online
View Journal

Cite this: DOI: 10.1039/d5qi02595h

Local symmetry engineering and Judd–Ofelt decoupling in $SrLaInO_4:Eu^{3+}$ for high-purity red emission toward advanced solid-state lighting

Weiwei Xiang,[a] Yuxiang Li,[a] Yongbin Hua,*[b] Li Li*[c] and Jae Su Yu *[a]

A highly efficient red phosphor, $SrLaInO_4:Eu^{3+}$ (SLIO:Eu^{3+}), was synthesized *via* a high-temperature solid-solution route for applications in near-ultraviolet (NUV) excited warm white light-emitting diodes (w-LEDs). Rietveld refinement verified that SLIO crystallizes in an orthorhombic $Pca2_1$ structure, where Eu^{3+} preferentially accommodates the low-symmetry La^{3+} site with a nine-coordinated [EuO_9] environment, effectively promoting the electric-dipole governed $^5D_0 \rightarrow {}^7F_2$ transition. Upon 395 nm excitation, the optimized composition (x = 0.20, in mol) delivers intense red emission centered at 615 nm, exhibiting a high color purity of 95%. The optimized phosphor had (0.659, 0.340) Commission Internationale de l'Eclairage chromaticity coordinates, approaching the National Television System Committee red standard. Concentration quenching is governed by a dipole–dipole interaction mechanism, with a calculated critical energy transfer distance of 12.89 Å. Judd–Ofelt spectral analysis yields a notably enhanced Ω_2 value, suggesting increased local structural asymmetry and a stronger covalent character around Eu^{3+}. The phosphor also featured a moderate luminescence decay time of 752 μs and a reduced optical band gap from 4.21 to 3.74 eV after Eu^{3+} incorporation with 2 mol. A warm w-LED fabricated using an NUV chip combined with SLIO:0.2Eu^{3+} and commercial blue/green phosphors achieved a correlated color temperature below 3100 K, demonstrating its strong promise as a high-performance red component for next-generation solid-state lighting based on phosphor-converted w-LEDs.

Received 24th December 2025,
Accepted 10th March 2026

DOI: 10.1039/d5qi02595h

rsc.li/frontiers-inorganic

1. Introduction

Recently, owing to their superior performances, including high luminous efficiency, long cycle life, low energy consumption, and high thermal and chemical stabilities, white light-emitting diodes (w-LEDs) have gained extensive interest.[1–4] Currently, commercial w-LEDs commonly contain a blue InGaN chip along with a yellow $Y_3Al_5O_{12}:Ce^{3+}$ (YAG:Ce^{3+}) phosphor.[5] Unfortunately, this configuration exhibits a poor color rendering index (CRI < 80) and a high correlated color temperature (CCT > 6000 K), resulting from the shortcoming of red-light content.[6,7] To solve these drawbacks, a possible alternative strategy is to develop multi-component red–green–blue (RGB) white-light systems by combining RGB phosphors with ultraviolet (UV) chips.[8] Compared with conventional YAG:Ce-based w-LEDs, the RGB phosphor approach enables broader and more balanced spectral coverage, providing improved color rendition, tunable CCT, enhanced luminous quality, and superior visual comfort for warm white lighting applications.[9]

Until now, extensive efforts have been taken to develop high-performance red-emitting phosphors based on rare-earth (RE) activators such as Eu^{2+}, Sm^{3+}, and Eu^{3+}.[10–12] Eu^{2+}-activated phosphors (*e.g.*, $CaAlSiN_3:Eu^{2+}$, $Sr_2Si_5N_8:Eu^{2+}$, *etc.*) exhibit broad-band emission released from the $4f^65d^1 \rightarrow 4f^7$ transition and have been widely used in commercial w-LEDs because of their high luminous efficiency.[13] However, their emission wavelengths are highly sensitive to the host lattice and crystal field strength, and their chemical stability is generally limited, especially in oxide environments. Similarly, Sm^{3+} phosphors can provide orange-red emission but usually suffer from relatively weak emission intensity and thermal quenching due to forbidden-transition features.[14] In contrast, Eu^{3+}-activated materials show narrow-band red emission dominated by the featured $^5D_0 \rightarrow {}^7F_J$ (J = 1–4) transitions, particularly the red $^5D_0 \rightarrow {}^7F_2$ (~610 nm) electric-dipole transition, which ensures excellent color purity and spectral stability.[15] In addition, Eu^{3+} exhibits excellent matrix compatibility, tunable site accommodation, and reliable thermal and chemical stability, giving it a significant advantage in next-generation warm w-LED applications.[16] To date, numerous Eu^{3+}-activated oxides and fluor-

[a]*Department of Electronic and Information Convergence Engineering, Institute for Wearable Convergence Electronics, Kyung Hee University, Yongin-si, Gyeonggi-do, 17104, Republic of Korea. E-mail: jsyu@khu.ac.kr*
[b]*School of Physics and Optoelectronic Engineering, Yangtze University, Jingzhou, 434023, China. E-mail: cdhyb@yangtzeu.edu.cn*
[c]*School of Electronic Science and Engineering, Chongqing University of Posts and Telecommunications, Chongqing, 400065, China. E-mail: lilic@cqupt.edu.cn*

ides have been investigated as red-emitting phosphors.[17] Among these hosts, oxide-based materials have gained particular interest thanks to their excellent chemical stability, reliable thermal reliability, and environmental safety compared to sulfides or nitrides.[18,19] Therefore, Eu^{3+}-doped red phosphors in oxide material systems have emerged as promising candidates to overcome the limitations of Eu^{2+} and Sm^{3+} ions and to achieve a high CRI with improved operational reliability.

Layered perovskite oxides with the general formula $AA'BO_4$ (A = alkaline earth metal; A′ = RE metal; B = trivalent cation, such as In^{3+}, Ga^{3+}, or Al^{3+}) have become ideal matrix materials for RE-activated phosphors in recent years.[20,21] The relatively rigid BO_6 octahedral framework ensures structural stability and mitigates thermal activation of phonon-assisted relaxation paths. Simultaneously, the flexible A/A′-site allows for stable incorporation and tunable local symmetry, thereby achieving controllable charge compensation, optimized energy levels, and electric dipole transitions for enhanced Eu^{3+} emission.[22] Due to their wide bandgap, high chemical stability, and favorable photophysical environment, $AA'BO_4$-type oxide is an ideal platform for designing red phosphors, which can be used in high-power solid-state lighting. $AA'BO_4$-type materials exhibited excellent performance and interesting phenomena, which have been widely reported. For example, $SrLaGaO_4$:Dy^{3+}/Eu^{3+}, $BaLaGaO_4$:Sm^{3+}, $CaGdGaO_4$:Bi^{3+}, $SrLaAlO_4$:Yb^{3+}, Er^{3+}, and $CaYAlO_4$:Dy^{3+} have been developed for use in the fields such as warm w-LEDs, blue light resource, and high sensitivity thermometers.[23–27]

Inspired by the aforementioned literature, we decided to introduce a $SrLaInO_4$ (SLIO) oxide, which has been reported mainly in the contexts of solar cells and electronic/photovoltaic applications.[28,29] In the luminescence area, the SLIO:Bi^{3+} phosphor has been reported as an X-ray-activated UV-A range persistent luminescent material, whereas its potential as an RE-activated phosphor remains largely underexplored.[30] Meanwhile, Eu^{3+}-activated $ALaBO_4$-type layered oxides have been explored as narrow-band emitters but most reports focus on phenomenological luminescence optimization and provide a limited quantitative linkage between crystallographic/site symmetry and hypersensitive electric-dipole emission.[31–34] A quantitative linkage between crystallographic site symmetry and Eu^{3+} hypersensitive emission behavior remains limited, as summarized in Table 1.

In this regard, SLIO offers an intrinsically low-symmetry A/A′-site framework that can accommodate Eu^{3+} in a nine-coordinated environment, enabling a symmetry-driven enhancement of the $^5D_0 \rightarrow {}^7F_2$ transition. Furthermore, by combining Rietveld refinement, spectroscopy, and Judd–Ofelt (J–O) analysis, we demonstrate a local-symmetry enhancement *vs.* lattice rigidity decoupling (enhanced Ω_2 with relatively stable Ω_4), providing a design principle beyond conventional dopant adjustment.[35] As an $AA'BO_4$-type oxide material, it provides a low-symmetry local environment for trivalent dopants (*e.g.*, Eu^{3+}), which is conducive to strong electric dipole transitions ($^5D_0 \rightarrow {}^7F_2$). Furthermore, the presence of Sr^{2+} and La^{3+} in the A/A′-site framework enables charge compensation and flexible lattice tuning, which is beneficial for stabilizing Eu^{3+} luminescent centers. In addition, indium (In)-based oxides possess a wide bandgap and good structural rigidity, making SLIO a promising matrix material for blue or near-UV (NUV) excited red phosphors.

In this work, by utilizing the solid-solution reaction method, a series of SLIO:$x$$Eu^{3+}$ phosphors were developed. The effects of Eu^{3+} content on the crystal structure, luminescence properties, decay behavior, and thermal stability were systematically studied. Site accommodation and local symmetry around Eu^{3+} ions were analyzed to elucidate the relationship between structural features and photoluminescence (PL) performance. The results demonstrate that SLIO:Eu^{3+} exhibits strong red emission under UV excitation, excellent color purity, and reliable thermal robustness, highlighting that it can be a promising material for warm w-LEDs and solid-state lighting applications.

2. Experimental section

2.1. Material synthesis

All the phosphor samples in this work were prepared *via* a conventional solid-state reaction method. An SLIO host and a series of $SrLa_{1-x}Eu_xInO_4$ (SLIO:$x$$Eu^{3+}$, x = 0.1, 0.2, 0.3, 0.4, and 0.5, in mol) phosphors were designed and synthesized. The nominal compositions were deliberately designed using a La-deficient incorporation strategy, in which the molar amount of La precursor was reduced by x and that of Eu precursor was increased correspondingly to maintain a constant A′-site incorporation. Accordingly, stoichiometric amounts of $SrCO_3$ (99%), La_2O_3 (99%), In_2O_3 (99%), and Eu_2O_3 (99%) were weighed based on the nominal $SrLa_{1-x}Eu_xInO_4$ compositions. The pre-

Table 1 Literature comparison of $SrLaInO_4$-related systems and several Eu^{3+}-activated $ALaBO_4$-type phosphors

System	Application focus	Main emission (nm)	CIE coordinates (x, y)	Symmetry-related analysis	Ref.
$SrLaInO_4$:Fe^{3+}	Solar cells	Not reported	Not reported	No	28
$SrLaInO_4$:Ti^{4+}	Ionic/proton conductivity	Not reported	Not reported	No	29
$SrLaInO_4$:Bi^{3+}	Persistent luminescence	565	Not reported	Qualitative	30
$BaLaInO_4$:Eu^{3+}	w-LEDs	612	(0.6321, 0.3669)	Qualitative	31
$BaLaGaO_4$:Eu^{3+}	w-LEDs and Plant growth	700	(0.6479, 0.3506)	J–O analysis (Brief)	32
$SrLaGaO_4$:Eu^{3+}	w-LEDs	618	(0.647, 0.353)	Qualitative	33
$SrLaAlO_4$:Eu^{3+}	Red phosphor	625	(0.6582, 0.3266)	Qualitative	34
$SrLaInO_4$:Eu^{3+}	w-LEDs	615	(0.6801, 0.3197)	J–O analysis (Structure-guided)	This work

cursors were thoroughly mixed and ground in an agate mortar for 30 min to ensure compositional homogeneity, followed by sintering at 1300 °C for 8 h in an alumina crucible under ambient air. After cooling to room temperature, the sintered products were ground into fine powders for subsequent characterization studies.

2.2. w-LED fabrication

w-LED devices were fabricated utilizing polydimethylsiloxane (PDMS) (silica epoxy gel A and B at a ratio of 10 : 1), the optimized SLIO:0.2Eu^{3+} phosphor, commercial $BaMgAl_{10}O_{17}$:Eu^{2+} blue phosphor (BAM:Eu^{2+}) and green $BaSc_2Si_3O_{10}$:Eu^{2+} phosphor (BSS:Eu^{2+}). For the w-LED device, 0.1 g of SLIO:0.2Eu^{3+} phosphor, 0.05 g of BAM:Eu^{2+}, and 0.07 g of BSS:Eu^{2+} were mixed with 1 g of PDMS solution. The as-prepared slurries were applied onto the 395 nm emitting chips and dried in an oven at 120 °C for 2 h.

2.3. Characterization studies

XRD analysis was performed on a Bruker D8 Advance diffractometer equipped with Cu Kα radiation (λ = 0.154056 nm) to determine the phase composition and crystal structure of the synthesized samples. The surface morphology and microstructural characteristics were analyzed using a high-resolution field-emission scanning electron microscope (HR-FESEM, Carl Zeiss), coupled with energy-dispersive X-ray spectroscopy (EDS) for elemental mapping and compositional investigation. The valence states and chemical environments of elements were characterized by X-ray photoelectron spectroscopy (XPS) on a Thermo Fisher Scientific K-Alpha spectrometer. PL excitation (PLE) and PL emission spectra were recorded using a Scinco FluoroMate FS-2 fluorescence spectrophotometer. The thermal durability of the as-obtained materials was evaluated by collecting temperature-dependent PL emission spectra from 303 to 483 K, controlled using a NOVA ST540 temperature-regulated stage.

2.4. Rietveld refinement details

Rietveld refinements of the XRD patterns were performed using the GSAS-II software.[36] The background was fitted using a polynomial function with 12 adjustable coefficients, and the peak profile was modeled using a pseudo-Voigt function, which is a linear combination of Gaussian and Lorentzian functions. During the refinement of structural information, fractional atomic coordinates (*e.g.*, 0, 1/8, 1/4, 1/3, 1/2, and 1) were fixed to their initial values, and only non-fractional atomic coordinates were refined.

3. Results and discussion

3.1. Structure and morphology

Fig. S1 of supporting information (SI) shows the powder XRD patterns of the SLIO host and all the SLIO:$x$$Eu^{3+}$ samples with different doping concentrations. When the dopant content x is lower than 0.3, all the diffraction peaks can be indexed to the standard SLIO phase (ICSD 169079), indicating single-phase formation in the low- and mid-doping range.[37] Considering the comparable valence states and ionic radius, Eu^{3+} ions (CN = 9, 1.12 Å) show a preference for the La^{3+} sites (CN = 9, 1.21 Å) rather than Sr^{2+} (CN = 9, 1.31 Å) or In^{3+} (CN = 6, 0.80 Å) sites.[12,23,38] This site preference can be further rationalized by calculating the ionic radius mismatch percentage according to the following formula:[10]

$$D_r = \frac{R_s - R_d}{R_s} \times 100\% \quad (1)$$

Here, R_s and R_d are the ionic radii of the acceptor and dopant ions, respectively. The as-obtained ionic radius mismatch (D_r) between Eu^{3+} and La^{3+} ions is 7.4%, which is far below the commonly accepted threshold of 30%, indicating that Eu^{3+} ions can be stably incorporated into the La^{3+} sites. As highlighted by the enlarged views near the (113) reflection, the diffraction peak shifts gradually toward higher 2θ angles with increasing Eu^{3+} content up to x = 0.3, consistent with lattice contraction induced by Eu^{3+} incorporation. When x is beyond 0.3, additional reflections attributable to secondary orthorhombic $EuInO_3$ with a *Pbnm* space group become visible.[39] Meanwhile, the (113) peak of the SLIO main phase shows a slight shift back toward lower angles, suggesting that the high Eu^{3+} ion concentration leads to phase separation, which reduces the effective Eu^{3+} incorporation in the remaining SLIO lattice. The Rietveld refinements of the XRD patterns for the as-obtained SLIO host and the optimal SLIO:0.2Eu^{3+} phosphor are illustrated in Fig. 1(a) and (b). All the diffraction peaks for both samples can be well matched with the standard pattern, confirming the successful synthesis process of the target phase and the effective integration of dopant Eu^{3+} ions into the SLIO lattice. To further analyze the crystal structure, Rietveld refinement was conducted utilizing GSAS-II, and the corresponding reliability factors are provided in Table S1 in the SI. The refinement parameters, including R_{wp} (6.85% and 7.26%), R_p (4.90% and 5.21%), and χ^2 (0.978 and 0.938), fall within acceptable ranges, indicating reliable refinement quality and high phase purity of the samples.[5] Fig. 1(c) shows the crystal structure of the SLIO:0.2Eu^{3+} phosphor and the corresponding polyhedral units. The SLIO host belongs to orthorhombic crystal system with a $Pca2_1$ space group. Upon incorporation of La^{3+} by slightly smaller Eu^{3+} ions, a subtle contraction of the crystal lattice occurs owing to the reduced ionic radius.[40] This observation is consistent with the refined cell volumes listed in Table S1 in the SI, where the lattice volume decreases from 433.625 $Å^3$ for the pristine SLIO host to 432.233 $Å^3$ at 0.2 mol Eu^{3+} doping.

To analyze the elemental composition and chemical states in SLIO:Eu^{3+} phosphors, XPS measurements were conducted over the binding energy range of 0–1350 eV, as shown in Fig. 2(a). Signals corresponding to Sr, La, In, Eu, and O were clearly detected, along with a minor C 1s peak at 284.8 eV, which was used for charge calibration.[41] The high-resolution spectra of individual elements are presented in Fig. 2(b–f). As depicted in Fig. 2(b), the Sr 3d spectrum exhibits two peaks at

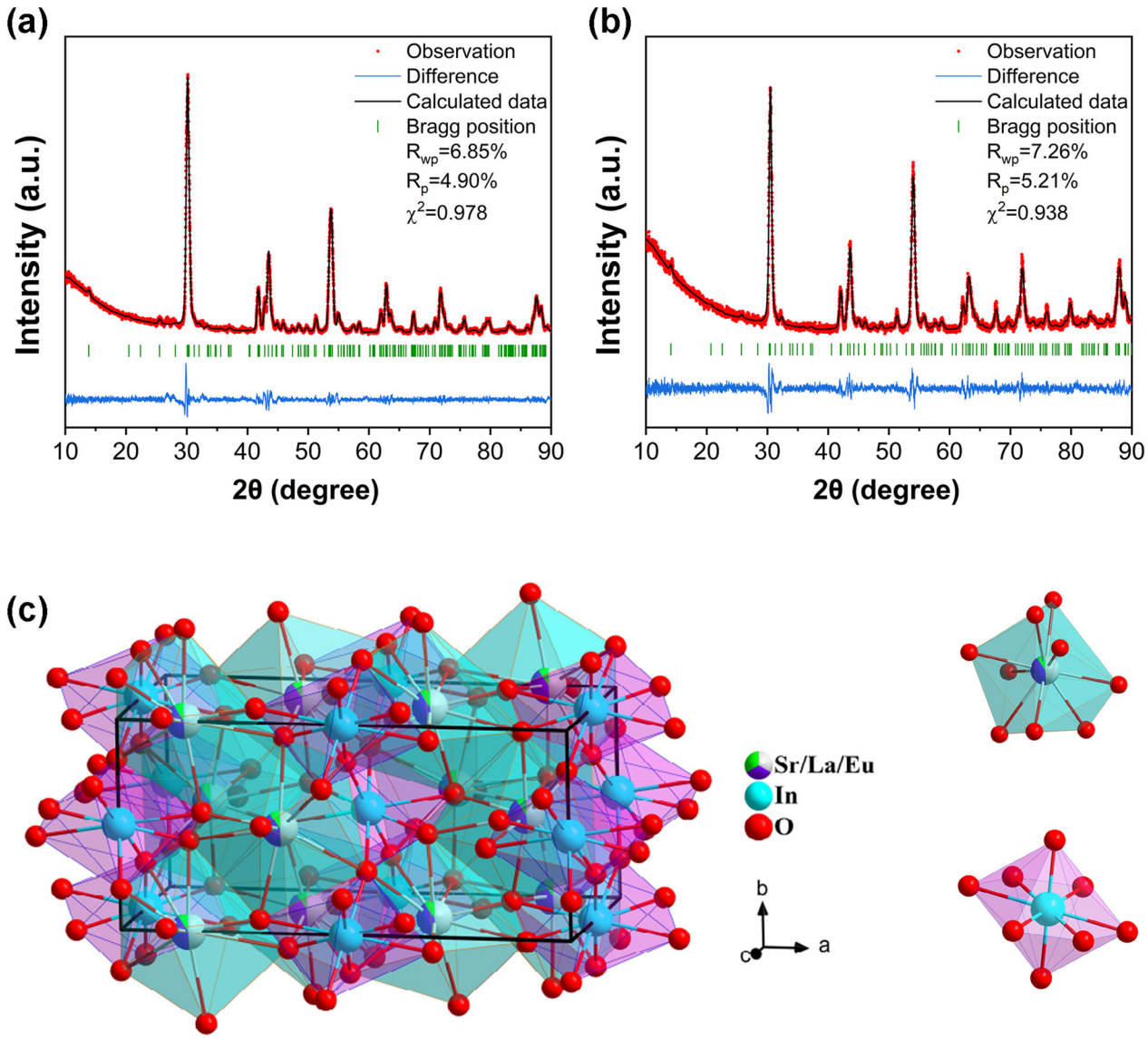

Fig. 1 Rietveld refinement of the XRD patterns for (a) the SLIO host and (b) the SLIO:0.2Eu^{3+} phosphor. (c) Schematic crystal structure of the SLIO and coordination environments of constituent cations.

134.75 and 132.94 eV, assigned to Sr $3d_{3/2}$ and Sr $3d_{5/2}$, respectively.[42] The La 3d spectrum (Fig. 2(c)) showed characteristic doublet features corresponding to La $3d_{3/2}$ (850.92 and 854.48 eV) and La $3d_{5/2}$ (834.17 and 837.72 eV).[24] The satellite peaks originate from the final-state charge-transfer process between La 3d core holes and La 4f/O 2p orbitals, giving rise to unscreened ($3d^94f^0$) and screened ($3d^94f^1L$) states (L denotes a ligand hole), consistent with La^{3+} in oxide environments.[43] As shown in Fig. 2(d), the In 3d spectrum exhibited two peaks at 451.20 and 443.65 eV, attributing to In $3d_{3/2}$ and In $3d_{5/2}$.[44] The Eu 3d core-level spectrum (Fig. 2(e)) showed two dominant peaks at 1162.90 and 1134.17 eV, attributed to Eu^{3+} $3d_{3/2}$ and $3d_{5/2}$, associated with the $3d^94f^6$ configuration.[42] The energy separation between the two peaks (28.73 eV) is consistent with literature values (~30 eV). Additional weak features at 1154.24 and 1125.19 eV are earmarked to Eu^{2+} $3d_{3/2}$ and $3d_{5/2}$, respectively.[11] Although no reducing environment was employed during synthesis, trace Eu^{2+} states can still appear, in agreement with previous reports on Eu-doped oxide material systems.[45] The O 1s spectrum (Fig. 2(f)) can be deconvoluted into three components peaked at 529.49, 531.21, and 533.39 eV, corresponding to lattice oxygen, oxygen vacancies, and surface-adsorbed oxygen species, respectively.[46]

The morphology of all the SLIO:*x*Eu^{3+} phosphors was measured by HR-FESEM analysis at 10 k×, and the corresponding images are presented in Fig. 3(a). All the samples exhibit similar morphological characteristics, consisting of irregularly shaped particles of sizes in the micrometer range and a certain degree of particle agglomeration, which is typical for phosphors synthesized *via* the high-temperature solid-state

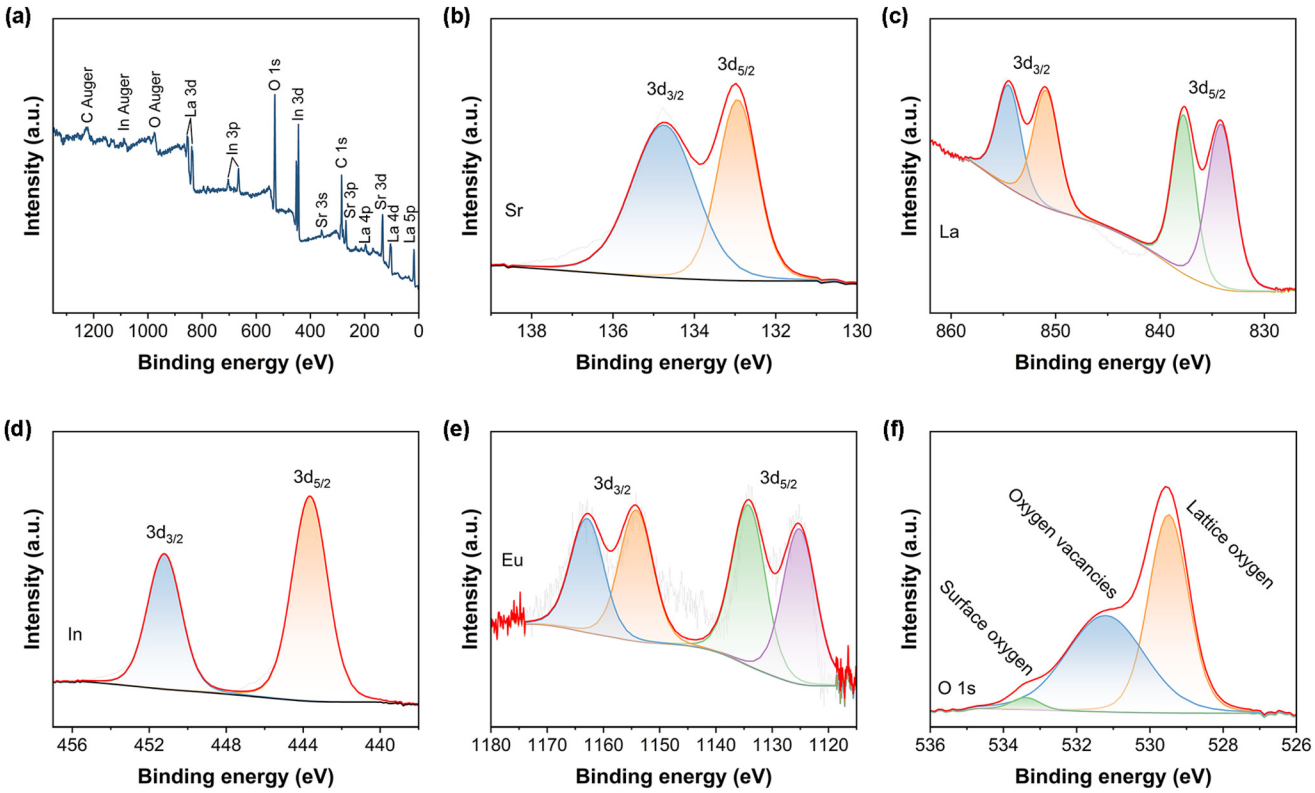

Fig. 2 (a) XPS survey scan spectrum and high-resolution core-level spectra (b–f) of Sr 3d, La 3d, In 3d, Eu 3d, and O 1s for the SLIO:0.2Eu^{3+} phosphor.

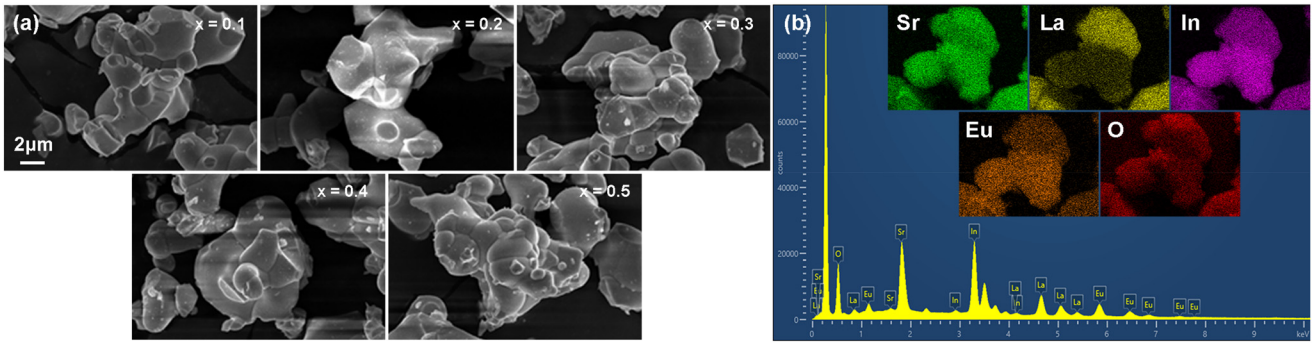

Fig. 3 (a) HR-FESEM micrographs of SLIO:xEu^{3+} phosphors at 10 kx. (b) EDS spectrum with elemental mapping images of Sr, La, In, Eu, and O (inset).

reaction method.[47] Notably, no obvious changes in particle morphology or grain size are observed with increasing Eu^{3+} ion concentration, indicating that Eu^{3+} doping has a negligible effect on the crystal growth behavior of the SLIO host. Although morphology can influence luminescence properties in some phosphor systems, the HR-FESEM results suggest that all the SLIO:xEu^{3+} samples possess very similar particle morphology and micro-scale grain sizes.[48,49] Therefore, morphology is unlikely to be the primary factor affecting the luminescence behavior in this work. The EDS spectrum shown in Fig. 3(b) confirmed the presence of Sr, La, In, Eu, and O elements in the sample. The homogeneous distribution of these elements, including Eu^{3+} dopant ions, is further verified by the elemental mapping images (inset of Fig. 3(b)), indicating that Eu^{3+} ions are successfully introduced into the SLIO host lattice without noticeable agglomeration or phase separation.

3.2. UV-Vis and band gap studies

The diffuse reflectance spectroscopy (DRS) spectra of the SLIO host and SLIO:0.2Eu^{3+} phosphor were recorded to explain the influence of Eu^{3+} incorporation on the optical absorption performance of the SLIO matrix, as presented in Fig. 4(a).

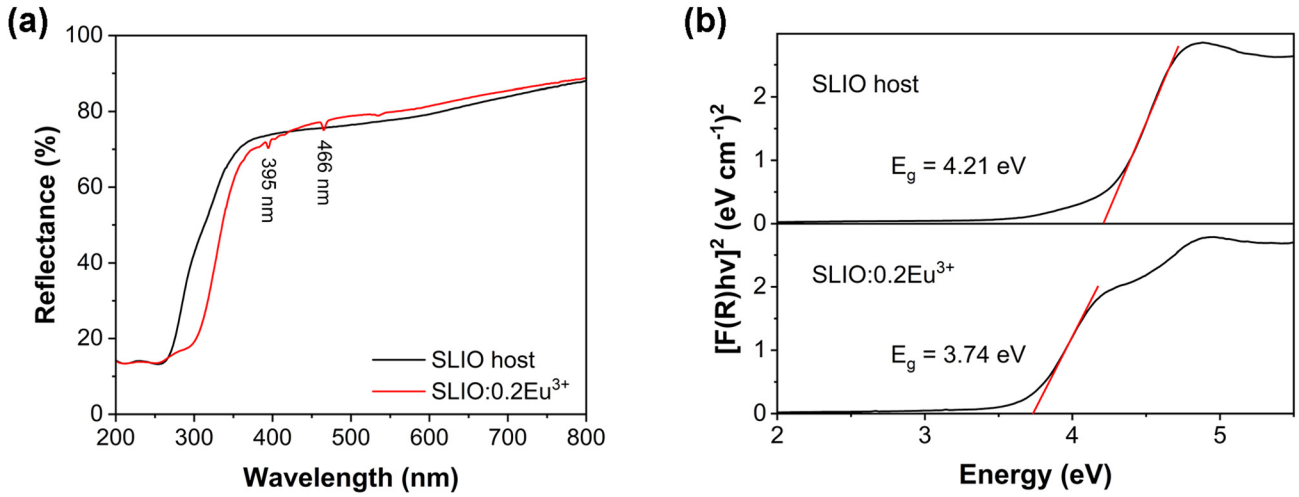

Fig. 4 (a) DRS spectra of the SLIO host and SLIO:0.2Eu^{3+} phosphor. (b) Tauc plots of the SLIO and SLIO:0.2Eu^{3+} phosphor.

Moreover, the optical band gap energy (E_g) was derived from the DRS data using the following equations:[50]

$$[F(R_\infty)h\nu]^{\frac{1}{n}} = A(h\nu - E_g) \quad (2)$$

$$[F(R_\infty)] = \frac{(1-R_\infty)^2}{2R_\infty} \quad (3)$$

Herein, R_∞ and $F(R_\infty)$ represent the reflectance coefficient and the Kubelka–Munk function, respectively, while h, ν, E_g, and A correspond to the Planck constant, photon frequency, band gap energy, and a proportion constant. The parameter n depends on the nature of the electronic transition: for direct allowed and direct forbidden transitions, n = 1/2 and 3/2, respectively, while for indirect allowed and indirect forbidden transitions, n = 2 and 3.[51] Since SLIO is a direct band gap material, n was taken as 1/2 in this work. As compared in Fig. 4(b), the estimated band energies of the un-doped SLIO host and the SLIO:0.2Eu^{3+} sample are approximately 4.21 and 3.74 eV, respectively. The results indicate that even a low concentration of Eu^{3+} doping leads to a narrowing of the band gap in SLIO, which is helpful to enhanced luminescence performance in the SLIO:Eu^{3+} phosphors.

3.3. PL properties

Fig. 5(a) shows the PL emission and PLE spectra of the optimal SLIO:0.2Eu^{3+} phosphor. PLE spectra, studied with the emission wavelength at 615 nm, released a broad band centered at 306 nm, corresponding to the $O^{2-} \rightarrow Eu^{3+}$ charge-transfer band (CTB).[16] In addition, several acute f–f transition peaks locating from 350 to 550 nm were observed at 364, 383, 395, 403, 415, 466, and 535 nm, attributing to the energy transitions from the Eu^{3+} ground state $^7F_0$ or $^7F_1$ to the excited states $^5G_{2,3}$, $^5L_6$, $^5D_4$, $^5D_3$, $^5D_2$, and $^5D_1$, respectively.[10] The emission spectrum exhibited characteristic Eu^{3+} emissions at 582, 595, 615, 657, and 707 nm, originating from the $^5D_0 \rightarrow {}^7F_J$ (J = 0–4) transitions.[32] As shown in Fig. 5(b), the phosphor showed strong red emission under excitations at 306, 395, and 466 nm, with 395 nm, located in the NUV range, indicating that the BLIO:Eu^{3+} phosphor can be excited by the commercial NUV chip. Fig. 5(c) shows the Eu^{3+} ion concentration-dependent PL emission spectra of SLIO:xEu^{3+}. All the PL excitation and emission spectra were recorded under a fixed excitation wavelength of 395 nm. The emission spectra collected under this condition were used for subsequent J–O analysis. The emission intensity initially increased and reached a maximum at x = 0.2, then gradually decreased with further Eu^{3+} addition. This trend is clearly demonstrated in Fig. 5(d), suggesting a concentration-dependent luminescence behavior. The decline beyond 0.2 mol Eu^{3+} is the result of concentration quenching. This means that exceeding dopant ion precipitate enables non-radiative energy transfer pathways, thereby reducing emission intensity.[22]

Three primary interaction mechanisms, including exchange interaction, electrostatic multipolar interaction, and radiative reabsorption, may contribute to concentration quenching in RE-activated phosphors. Radiative reabsorption typically occurs when there is a significant overlap between the PL emission and PLE spectra.[52] As no obvious overlap was observed for the SLIO:Eu^{3+} phosphors, the concentration quenching behavior is mainly governed by exchange or electrostatic multipolar interactions, rather than radiative reabsorption. To further understand the quenching mechanism, the critical distance (R_c) between Eu^{3+} activators was estimated based on the Blasse theory using the following equation:[46]

$$R_c = 2\left(\frac{3V}{4\pi x_c Z}\right)^{1/3} \quad (4)$$

Here, V (unit-cell volume), x_c (critical dopant concentration), and Z (number of cation sites per unit cell) are parameters for determining the critical distance. For the SLIO:Eu^{3+} phosphors, V = 449.35 Å^3, x_c = 0.2, and Z = 2. Based on these parameters, the critical distance (R_c) between Eu^{3+} ions was

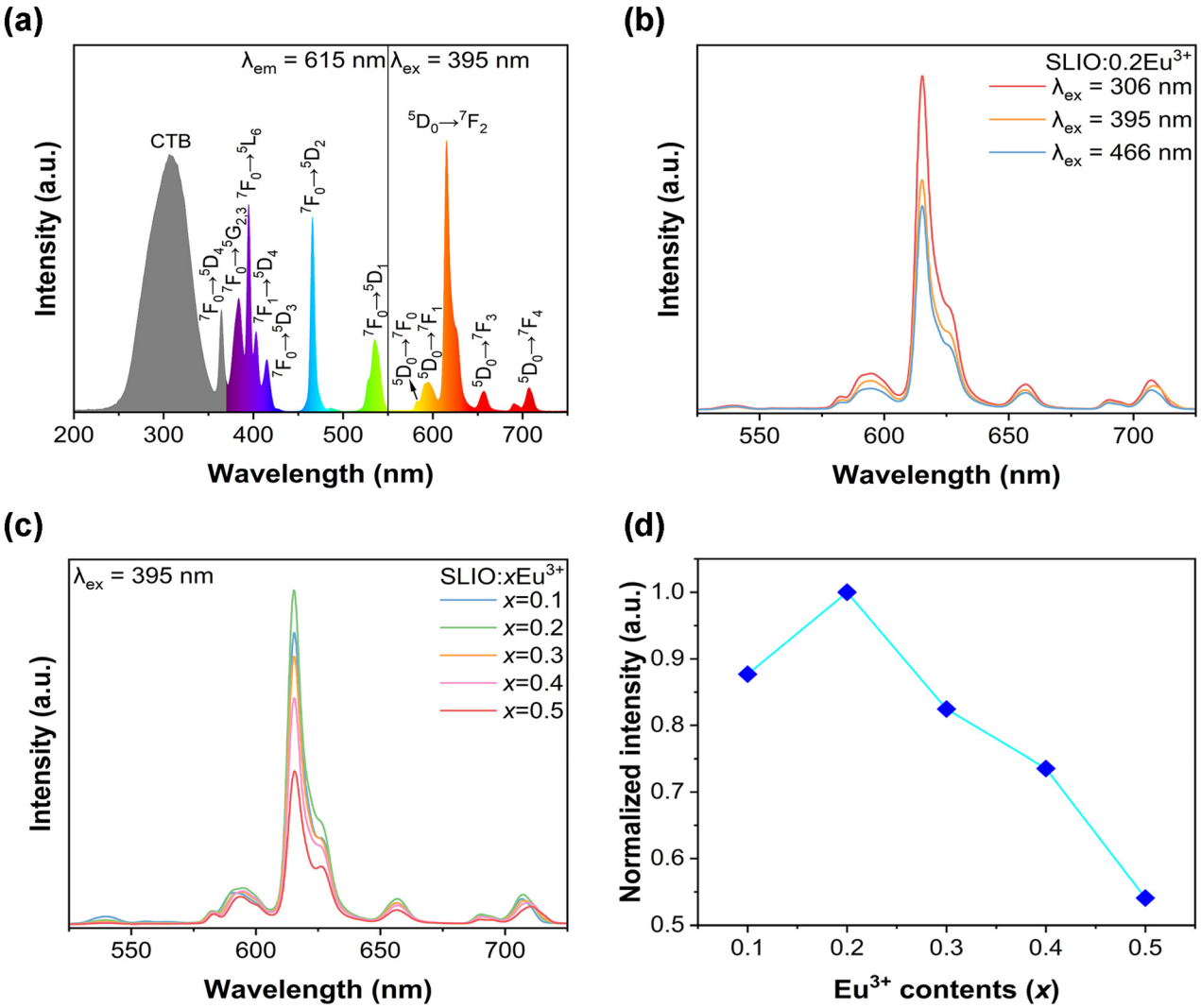

Fig. 5 (a) Excitation and emission spectra of the SLIO:0.2Eu^{3+} phosphor. (b) Emission spectra of the SLIO:0.2Eu^{3+} phosphor at different excitation wavelengths. (c) Eu^{3+} ion concentration-dependent PL emission spectra. (d) Normalized emission intensity as a function of dopant content.

obtained to be 12.89 Å. Since exchange interaction typically dominates when R_c < 5 Å, the significantly larger R_c value obtained in this work implies that the concentration-quenching process is mainly governed by electrostatic multipolar interactions rather than exchange interactions.[15] For electrostatic multipolar interactions, three types of interactions may occur (dipole–dipole (d–d), dipole–quadrupole (d–q), and quadrupole–quadrupole (q–q)). The dominant mechanism is determined by analyzing the interaction parameter Q according to the following relation:[18]

$$\frac{I}{x} = k(1 + \beta(x)^{Q/3})^{-1} \quad (5)$$

In this expression, x and I mean the dopant concentration and the corresponding PL emission intensity, respectively. According to the theoretical model, the dominant interaction mechanism is associated with the value of the parameter Q: d–d, d–q, and q–q interactions correspond to Q values of 6, 8, and 10, respectively. When x exceeds the critical concentration (x_c), the above relationship can be linearized and rewritten as eqn (3):[17]

$$\log\left(\frac{I}{x}\right) = C - (Q/3)\log(x) \quad (6)$$

Based on this equation, the linear fitting of the log(I/x) *versus* log(x) plot is shown in Fig. 6(a). The slope is determined to be −1.81, corresponding to a calculated Q value of approximately 5.43, close to 6, showing that the concentration-quenching behavior of SLIO:Eu^{3+} phosphors is predominantly governed by d–d interactions. In addition to multipolar interactions, particle morphology can also influence luminescence behavior by affecting light scattering and surface-related non-radiative processes.[53,54] However, since all the samples exhibit very similar particle morphology and comparable grain sizes, the influence of morphology on the concentration-dependent PL properties is expected to be minimal in the present system.

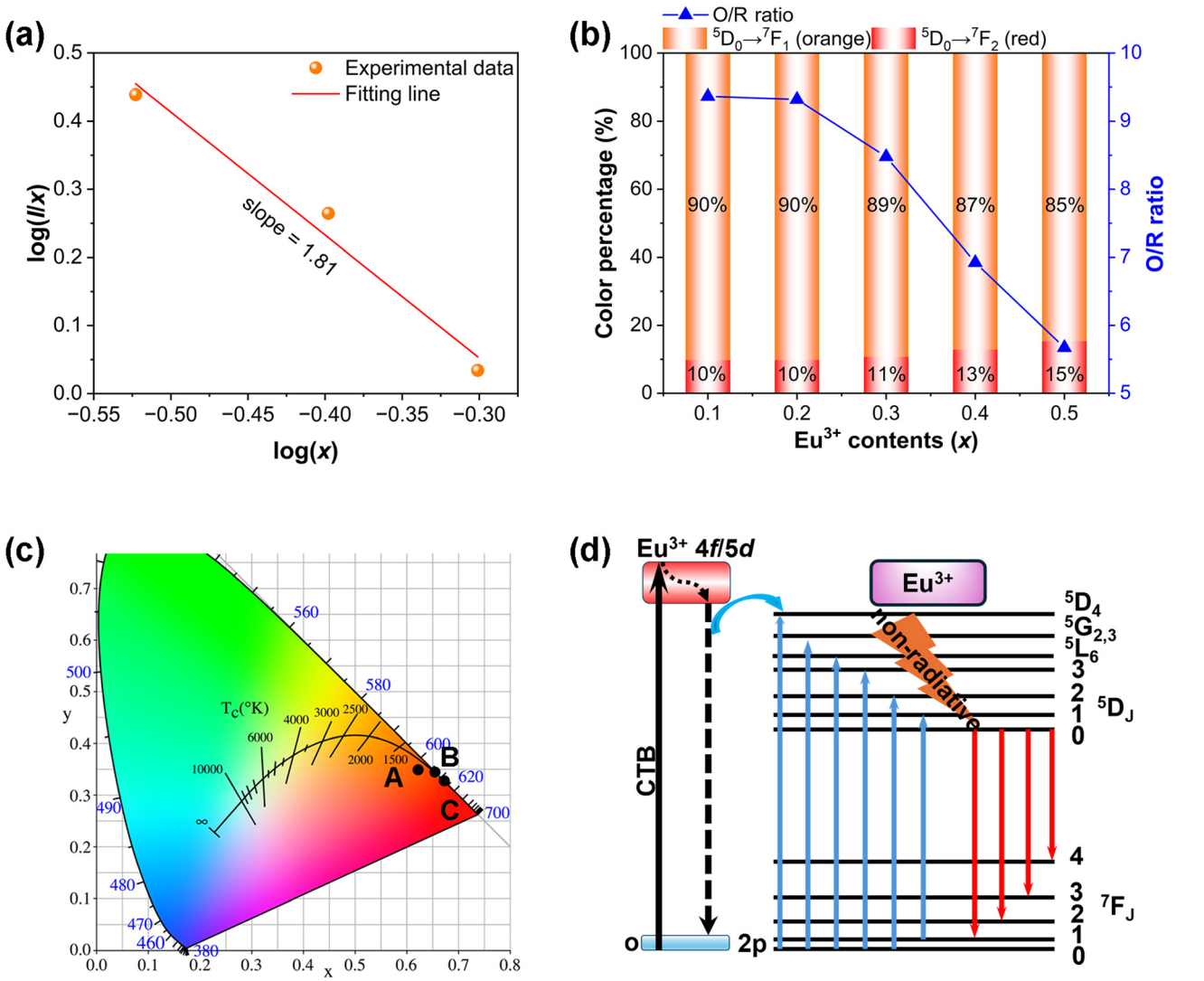

Fig. 6 (a) Log(*I*/*x*) *vs.* log(*x*) dependence with linear fitting. (b) Variation of orange/red emission components and O/R ratio with Eu^{3+} content. (c) CIE chromaticity coordinates of the SLIO:0.2Eu^{3+} phosphor with NTSC standard red and commercial $Y_2O_2S:Eu^{3+}$ phosphors. (d) Proposed energy-level scheme of Eu^{3+} in the SLIO host.

The evolution of the magnetic-dipole (MD, $^5D_0 \rightarrow {}^7F_1$) and electric-dipole (ED, $^5D_0 \rightarrow {}^7F_1$) transition percentages plotted against Eu^{3+} ion concentration is presented in Fig. 6(b).[55] With increasing Eu^{3+} content, the orange-to-red emission ratio (O/R) gradually increased, indicating a modification of the local crystal field environment surrounding Eu^{3+} ions. Typically, the $^5D_0 \rightarrow {}^7F_1$ transition is a parity-allowed MD transition, and its intensity is nearly insensitive to the site symmetry. In contrast, the $^5D_0 \rightarrow {}^7F_2$ transition is a hypersensitive ED transition, strongly dependent on the asymmetry of the local coordination environment. As more Eu^{3+} ions preferentially accommodate La^{3+} lattice sites, the inversion symmetry around the Eu^{3+} centers becomes increasingly disrupted, leading to the enhancement of the ED transition. Consequently, the emission shifts toward the dominant $^5D_0 \rightarrow {}^7F_2$ red-emission band, suggesting a gradual color evolution toward red with increasing Eu^{3+} ion concentration.

Fig. 6(c) shows the Commission Internationale de l'Eclairage (CIE) chromaticity coordinates of the Eu^{3+}-activated SLIO phosphor at the optimal dopant content. Based on the PL spectra, the chromaticity point of the SLIO:0.2Eu^{3+} sample is calculated to be (0.659, 0.340), which is very close to the National Television System Committee (NTSC) standard for red emission (0.670, 0.330).[56] This value is also better than the widely used commercial $Y_2O_2S:Eu^{3+}$ phosphors (0.622, 0.351), highlighting the excellent CRI capability of the present material. To further assess the color performance, the color purity was calculated, which can be defined as follows:[20]

$$\text{Color purity} = \sqrt{\frac{(x - x_i)^2 + (y - y_i)^2}{(x_d - x_i)^2 + (y_d - y_i)^2}} \times 100\%. \quad (7)$$

In this equation, (x, y), (x_i, y_i), and (x_d, y_d) represent the chromaticity coordinates of the phosphor, the standard white

light source, and the dominant wavelength point, respectively. The coordinates of the white point and the dominant wavelength (615 nm) are taken as $(x_i, y_i) = (0.310, 0.316)$ and $(x_d, y_d) = (0.6801, 0.3197)$, respectively.[6] The CIE chromaticity coordinates of SLIO:xEu^{3+} under 306 and 395 nm excitations are listed in Tables S2 and S3 in the SI, respectively. As the Eu^{3+} ion concentration increased, the calculated color purity showed a consistent enhancement under both excitation wavelengths, which is in agreement with the previous O/R ratio analysis, confirming the progressive strengthening of the $^5D_0 \rightarrow {}^7F_2$ transition with increasing Eu^{3+} content. In addition to chromaticity and color purity, CCT is another important parameter used to evaluate the warmth or coolness of emitted light. Generally, CCT values below 3000 K correspond to warm white light, whereas the values above 4000 K indicate cold white emission. CCT can be obtained by the following equation:[23]

$$\mathrm{CCT} = -437n^3 + 3601n^2 - 6861n + 5514.31 \quad (8)$$

Here, n is calculated based on the inverse slope and the chromaticity epicenter using McCamy's empirical formula:

$$n = \frac{x - x_e}{y - y_e} \quad (9)$$

where x_e and y_e correspond to the chromaticity coordinates of the reference black-body radiation point in the CIE diagram, which are 0.3320 and 0.1858, respectively. As summarized in Tables S2 and S3 in the SI, the CCT values of SLIO:xEu^{3+} phosphors under both 306 nm and 395 nm excitations fall within the range of 2800–3100 K. This indicates that the phosphors exhibit warm light characteristics, which is advantageous compared to conventional high-CCT cold light sources that often cause visual discomfort and reduce lighting quality. The combined results, which include favorable chromaticity coordinates, high color purity, and desirable warm light CCT, demonstrate that Eu^{3+}-activated SLIO phosphors possess excellent luminescence properties. Therefore, these materials hold strong potential as promising red-emitting candidates for warm w-LEDs applications.

Fig. 6(d) presents the schematic energy-level diagram of Eu^{3+} ions in the SLIO host, illustrating the excitation and emission processes. Upon excitation with high-energy photons, electrons in Eu^{3+} are promoted from the ground state $^7F_0$ to higher lying $4f^6 5d$ or ^5L and ^5D manifold states. These excited electrons subsequently release non-radiatively to the lowest excited state $^5D_0$, followed by radiative transitions to the ^7F_J (J = 0–4) multiple levels, giving rise to the characteristic Eu^{3+} emission lines. The excitation spectrum confirms that the phosphor can be effectively excited by NUV commercial LED chips, highlighting its potential for solid-state lighting applications. An equation is used to fit the decay curve:[10]

$$I = I_0 + A\exp\left(\frac{-t}{\tau}\right) \quad (10)$$

where I and I_0 are the luminescence intensities at the times of t = 0 and t, respectively, A is a constant, and τ is the lifetime. Generally, if the decay time τ can be single-exponential, indicating that there is only one radiative pathway governing this system, and the luminescent centers are in the same coordinate environment.[57] The contribution of non-radiative channels is constant and avoids significant energy transfer, cross-relaxation, or defect quenching competition. Otherwise, there are at least two different attenuation paths or luminescence center environments. As shown in Fig. 7(a), as the Eu^{3+} doping concentration continuously increases, their decay time has a trend of decline. This phenomenon can be attributed to the reduced interionic distance between Eu^{3+} ions with increasing doping concentration, which promotes more frequent energy transfer among dopant ions and thus enhances the probability of non-radiative transitions.[58] Moreover, all the decay curves were well-fitted with a single-exponential express, implying that Eu^{3+} ions take the same local lattice environment in the SLIO lattice.

3.4. J–O analysis

The J–O analysis was performed using emission spectra measured under identical excitation conditions (λ_{ex} = 395 nm). The J–O theory gives an effective method for evaluating the local symmetry environment and radiative characteristics of RE ions in solid hosts using a JOES software.[35] The three intensity parameters (Ω_2, Ω_4, and Ω_6) reflect the structural and bonding characteristics of the host lattice.[59] Among them, Ω_2 is highly sensitive to the site symmetry and covalency; lower Ω_2 values typically correspond to more centrosymmetric environments, while an increase in Ω_2 indicates reduced local symmetry and enhanced covalent interaction between Eu^{3+} ions and surrounding O^{2-} ligands. In contrast, Ω_4 and Ω_6 are not directly governed by symmetry but are more strongly influenced by the rigidity, viscosity, and packing density of the host framework, as well as vibronic coupling between Eu^{3+} and its coordinating ligands. Although their physical interpretation is less explicit than that of Ω_2, these two parameters provide valuable insight into the bulk structural properties and lattice dynamics of the matrix. The J–O intensity parameters are commonly derived from transition intensity analysis in PL spectra. In this experiment, they are evaluated based on the intensity ratios between the ED transitions $^5D_0 \rightarrow {}^7F_J$ (J = 2, 4, and 6) and the MD reference transition $^5D_0 \rightarrow {}^7F_1$, as expressed in eqn (11).[60] These spectral transitions form the foundation for collecting the J–O parameters and further evaluating the radiative behavior of Eu^{3+} ions in the host lattice:

$$R = \frac{\int I_J \mathrm{d}\nu}{\int I_1 \mathrm{d}\nu} = \frac{n(n^2+2)^2 e^2 {\nu_J}^3}{9n^3 S_{MD} {\nu_1}^3} \Omega_\lambda \left\langle {}^5D_0 \middle\| U^{(\lambda)} \middle\| {}^7F_J \right\rangle^2 \quad (11)$$

In this equation, ν_1 corresponds to the wavenumber of the MD transition $^5D_0 \rightarrow {}^7F_1$, while ν_J represents the wavenumbers of the ED transitions $^5D_0 \rightarrow {}^7F_J$ (J = 2, 4, and 6). The term S_{MD} is the MD transition line strength of Eu^{3+} ions, with a constant value of 9.6×10^{-42} esu^2 cm^2, which is considered independent of the host lattice. I_1 and I_J denote the integrated emission intensities of the $^5D_0 \rightarrow {}^7F_1$ and $^5D_0 \rightarrow {}^7F_J$ transitions, respectively. The squares of the reduced matrix elements of the unit tensor operator terms $\left\langle {}^5D_0 \middle\| U^{(\lambda)} \middle\| {}^7F_J \right\rangle^2$ are introduced from the

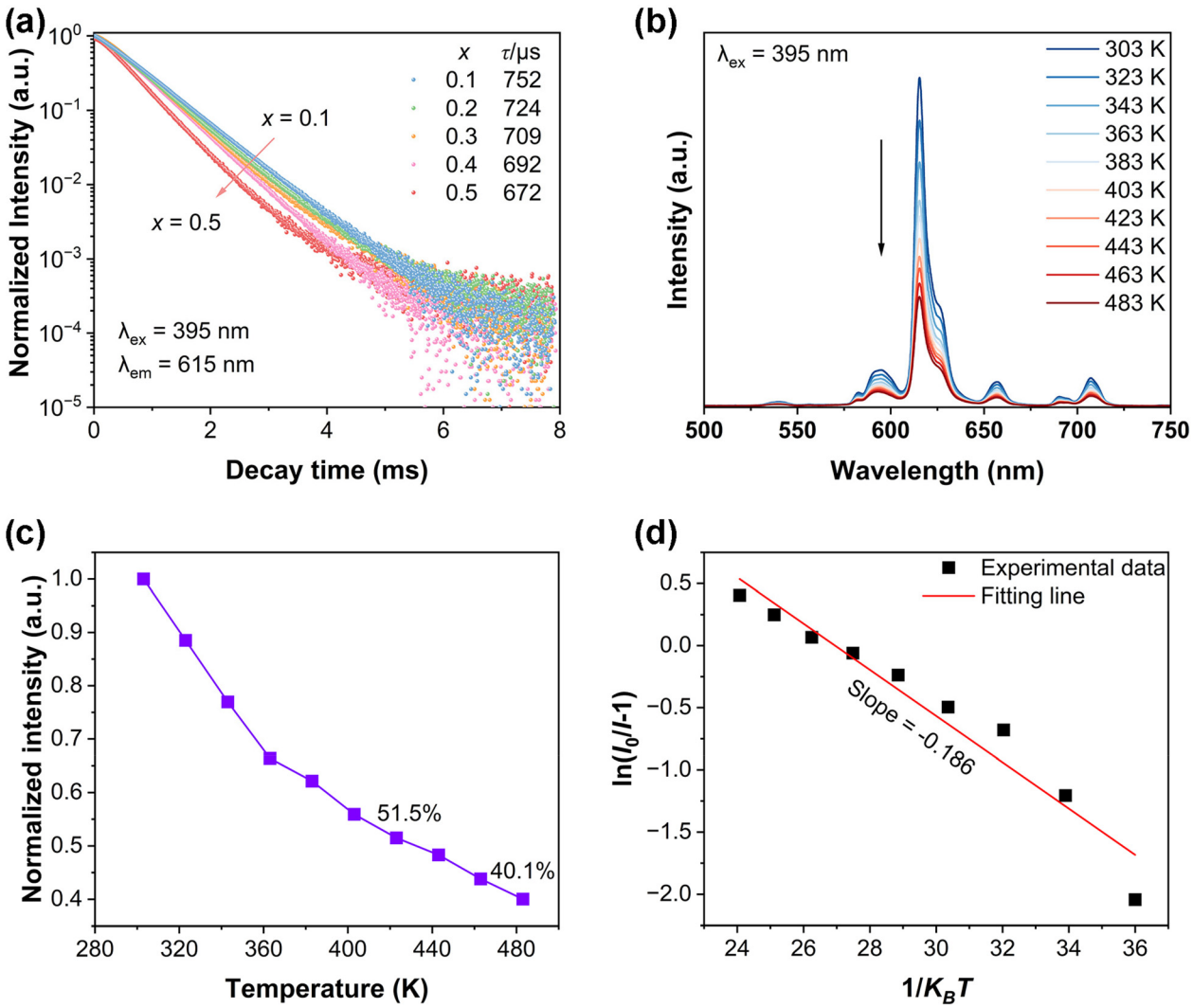

Fig. 7 (a) Luminescence decay time of SLIO:xEu^{3+} phosphors. (b) Temperature-dependent PL emission spectra. (c) Normalized integrated emission intensity at different temperatures. (d) $\ln(I_0/I - 1)$ *vs.* $1/K_BT$ plot and linear fitting.

table values reported by Carnall *et al.*[61] In addition, the index of refraction n of the host matrix is estimated using the Lorentz–Lorenz relation, which provides an effective approach for related optical polarization with the local dielectric environment of the material:[62]

$$\frac{n^2-1}{n^2+2}\frac{1}{\rho}=\frac{\sum l_i r_i}{M} \quad (12)$$

In the Lorentz–Lorenz equation, l_i is the number of electrons of the composition element in the material chemical formula, M is the molar mass of the compound, r_i is the molar refraction, and ρ is the theoretical density. Based on this relationship, n of the host lattice was estimated to be 2.002. Owing to the characteristic 4f–4f energy level configuration of Eu^{3+} ions, the J–O intensity parameters Ω_2 and Ω_4 can be reliably derived from the emission spectra. However, the $^5D_0 \rightarrow {}^7F_6$ transition was not monitored in the PL spectra in this work, preventing the determination of Ω_6. Herein, the Ω_2 and Ω_4 parameters for Eu^{3+}-activated SLIO phosphors were calculated using the JOES software package, with the refractive index (n = 2.002) obtained from the Lorentz–Lorenz equation. The practical Eu^{3+} molar concentrations incorporated into the host lattice are summarized in Table 2. Among the J–O parameters, Ω_2 is strongly correlated with the hypersensitive ED transition $^5D_0 \rightarrow {}^7F_2$ and provides key information on the covalency of the Eu–O bond as well as the asymmetry of the local crystal field around Eu^{3+} ions. In contrast, Ω_4 is more sensitive to the rigidity and electron density distribution of the surrounding ligand framework, where a higher Ω_4 generally indicates reduced ligand electron density. The larger Ω_2 values compared to Ω_4 in SLIO imply that Eu^{3+} ion priority accommodates low-symmetry and highly covalent coordination environments, which agrees with the dominant hypersensitive $^5D_0 \rightarrow {}^7F_2$ emission observed in PL spectra. This conclusion is in good agreement with the nephelauxetic effect and current reports, and larger Ω_2 values indi-

Table 2 J–O intensity parameters, asymmetry ratio, and branching ratio of SLIO:xEu^{3+} phosphors

x (mol)	Ω_2 ($\times 10^{-20}$ cm^2)	Ω_4 ($\times 10^{-20}$ cm^2)	Asymmetric ratio (R)	β_{calc} (%) for $^5D_0 \rightarrow {}^7F_2$ transition
0.1	9.493	2.329	6.242	78.4
0.2	9.517	2.294	6.249	78.6
0.3	9.388	2.323	6.176	78.3
0.4	9.077	2.302	5.975	77.8
0.5	8.817	2.276	5.804	77.4

cate increased nephelauxetic effect (reduced Racah B), confirming stronger Eu–O covalency. In this study, Ω_2 ranges from 8.817 to 9.517 $\times$ 10^{-20} cm^2, while Ω_4 varies from 2.276 to 2.329 $\times$ 10^{-20} cm^2. The relatively close magnitude and small variation of these parameters imply that neither the local coordination asymmetry around Eu^{3+} ions nor the ligand electron density undergoes significant alteration with increasing dopant concentration.

The radiative transition probability in J–O analysis is evaluated based on the $^5D_0 \rightarrow {}^7F_J$ (J = 1, 2, 4, and 6) transitions, while the $^5D_0 \rightarrow {}^7F_0$, $^5D_0 \rightarrow {}^7F_3$, and $^5D_0 \rightarrow {}^7F_5$ transitions are parity-forbidden and thus excluded from the analysis. As mentioned above, the $^5D_0 \rightarrow {}^7F_6$ emission was not observed in the PL spectra, making the intensity parameter Ω_6 neglected in SLIO:xEu^{3+} phosphors. Consequently, only the $^5D_0 \rightarrow {}^7F_1$, $^5D_0 \rightarrow {}^7F_2$, and $^5D_0 \rightarrow {}^7F_4$ transitions are considered for calculating the radiative transition probabilities. For Eu^{3+} ions, ED transitions originating from the $^5D_0$ level exhibit zero reduced matrix elements except for a few hypersensitive transitions, namely $^5D_0 \rightarrow {}^7F_2$ (U^2 = 0.0032), $^5D_0 \rightarrow {}^7F_4$ (U^4 = 0.0023), and $^5D_0 \rightarrow {}^7F_6$ (U^6 = 0.0002).[63] Among these, the first two transitions are utilized. The spontaneous radiative transition probability (A) correlated with the ED component can be expressed as formulated as follows:[60]

$$A(J,J') = \frac{64\pi^4 V^3}{3h(2J+1)}[\chi_{MD}S_{MD} + \chi_{ED}S_{ED}] \quad (13)$$

where h is Planck's constant, S_{MD} and S_{ED} are the MD and ED transition strengths, while χ_{MD} and χ_{ED} denote the local field correction factors corresponding to MD and ED transitions. Eqn. (14) and (15) are employed to get the correction factors using the refractive index (n):[64]

$$\chi_{MD} = n^3 \quad (14)$$

$$\chi_{ED} = \frac{n(n^2+2)^2}{9} \quad (15)$$

The J–O intensity parameters were employed to calculate the S_{ED} using eqn (16), while the S_{MD} remained a constant value of 9.6 $\times$ 10^{-42} esu^2 cm^2, independent of the host matrix:

$$S_{ED} = e^2 \sum_{J=2,4,6} \Omega_\lambda \left\langle {}^5D_0 \middle\| U^{(\lambda)} \middle\| {}^7F_J \right\rangle^2 \quad (16)$$

The calculated radiative transition probability $A(J, J')$, along with the total radiative transition probability $\sum A(J, J')$ or A_r derived from the J–O intensity parameters (Ω_2 and Ω_4), is summarized in Table 2. Based on these radiative transition probabilities, the branching ratio β_{calc} for each transition can be determined using the following equation:[58]

$$\beta_{calc}(\%) = \frac{A(J,J')}{\sum A(J,J')} \times 100 \quad (17)$$

As summarized in Table 2, across all the Eu^{3+} ion concentrations investigated (0.1–0.5 mol), the branching ratio of the most dominant transition $^5D_0 \rightarrow {}^7F_2$ falls within the range of 77.4%–78.6%.

According to previous reports, a branching ratio exceeding 50% suggests that the corresponding transition has the potential to support laser emission. In addition, the quantum efficiency, a crucial parameter for evaluating phosphor performance, can be determined using the following equation:[65]

$$\eta_{QE} = \frac{\tau}{\tau_r} \times 100\% \quad (18)$$

where τ is the experimental lifetime and τ_r is the calculated radiative lifetime. As shown in Table S4 in the SI, the η_{QE} values of SLIO:xEu^{3+} phosphors are high, indicating that radiative transition is the predominant pathway while non-radiative losses remain limited. What should be emphasized is that some of the η_{QE} values exceed 100%, which is physically unrealistic and does not imply photon yields greater than unity.[54] Such results originate from the inherent assumptions of J–O analysis. In particular, these deviations may arise from the neglect or underestimation of weak non-radiative relaxation pathways, the potential overestimation of radiative transition probabilities associated with large Ω_2 parameters in highly distorted coordination environments, and decay time measurements that may be affected by energy migration or the site-selective emission process.[58] In this framework, a η_{QE} over 100% only suggests that the radiative decay dominates and that non-radiative contributions are negligible within the limitations of the J–O model. In summary, the η_{QE} values derived from J–O analysis remain consistent with the structural and optical characteristics discussed in this work.

Overall, the J–O analysis confirms that Eu^{3+} ions accommodate non-centrosymmetric and moderately covalent environments in the SLIO lattice, with stable local coordination unaffected by dopant concentration, which is consistent with the high red emission efficiency and strong $^5D_0 \rightarrow {}^7F_2$ transition majority. When compared with representative reports summarized in Table 1, the present SLIO:Eu^{3+} material system distinguishes itself by quantitatively linking local symmetry to luminescence behavior through a structure-guided J–O analysis.

3.5. Thermal stability

To assess the thermal stability of SLIO:Eu^{3+} phosphors, temperature-dependent PL emission spectra of the optimally doped sample were monitored in the range of 303–483 K, as shown in Fig. 7(b). With increasing temperature, the PL intensity gradually decreased due to thermal quenching, while the peak posi-

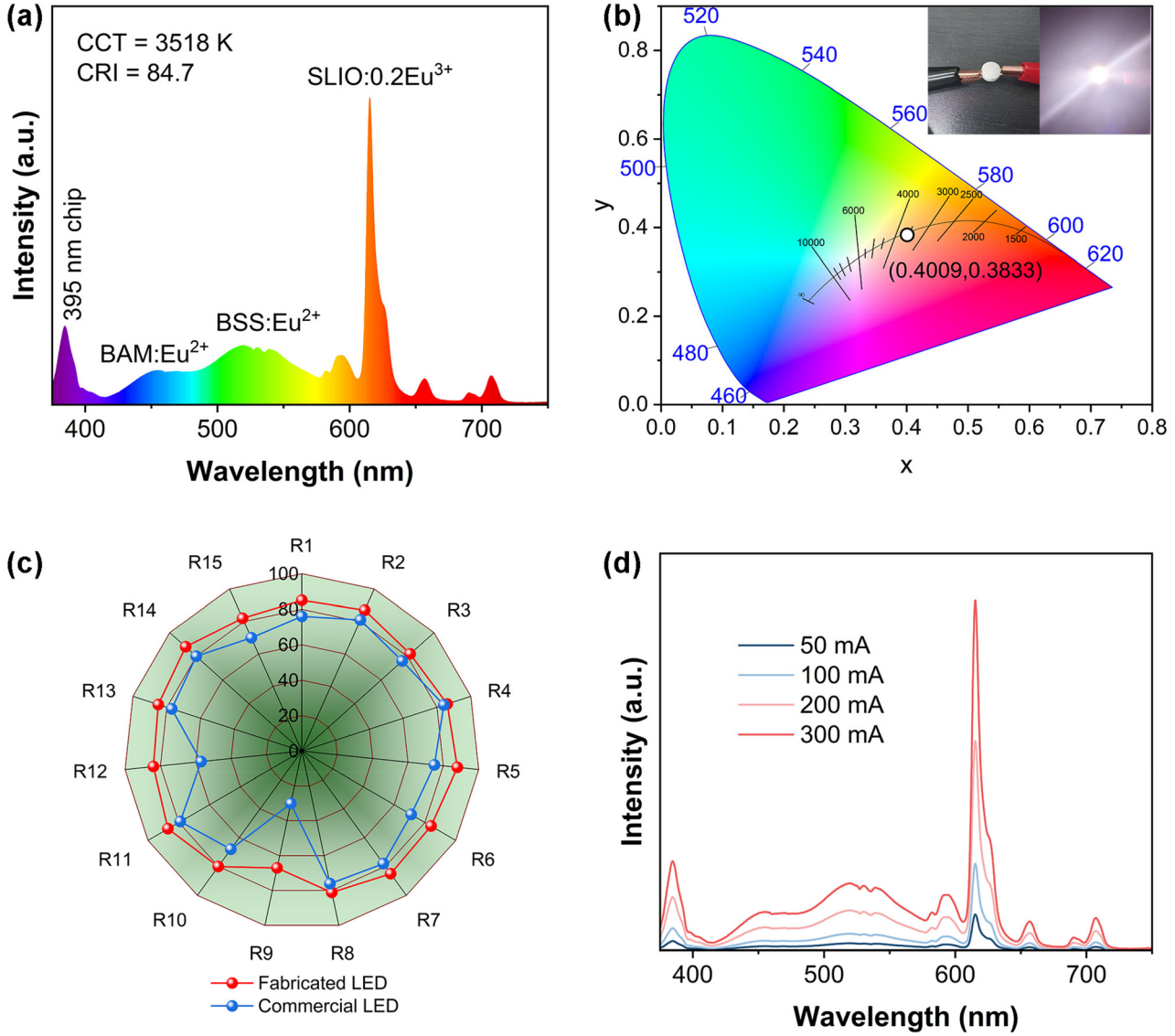

Fig. 8 (a) EL spectrum of the fabricated w-LEDs. (b) CIE chromaticity coordinates (inset: device photograph). (c) Color-rendering comparison with a commercial w-LED. (d) Emission spectra under different driving currents.

tions remained unchanged, suggesting that the emission centers are stable under thermal excitation. The reduction in emission intensity at elevated temperature is mainly attributed to enhanced non-radiative relaxation processes that compete with radiative transitions. The normalized integrated emission intensities as a function of temperature are plotted in Fig. 7(c). Based on the temperature-dependent luminescence behavior, the activation energy (ΔE) for thermal quenching was evaluated using the Arrhenius equation:[41]

$$I = \frac{I_0}{1 + c\ \exp\left(-\frac{\Delta E}{K_B T}\right)} \tag{19}$$

In this equation, c is a constant, I_0 denotes the emission intensity at room temperature, and I is the luminescence intensity at temperature T. The Boltzmann constant is represented by K_B (8.63×10^{-5} eV K^{-1}). As illustrated in the figure, the Arrhenius expression can be rearranged into a linear form, yielding a plot of $\ln(I_0/I - 1)$ *versus* $1/K_B T$, which enables the determination of the activation energy for thermal quenching:

$$\ln\left(\frac{I_0}{I} - 1\right) = -\frac{\Delta E}{K_B T} + \ln c \tag{20}$$

The dependence between $\ln(I_0/I - 1)$ and $1/K_B T$ is shown in Fig. 7(d). It can be seen that the ΔE value was obtained to be 0.186 eV for the SLIO:0.2Eu^{3+} phosphor as the slope is −0.186.

3.6. w-LED application

To evaluate the practical applicability of the synthesized SLIO:Eu^{3+} phosphors in solid-state lighting, a warm w-LED prototype was fabricated by combining SLIO:Eu^{3+} with commercial

BAM:Eu^{2+} and BSS:Eu^{2+} phosphors, coating the phosphor blend onto a 395 nm NUV LED chip. The electroluminescence (EL) spectrum of the packaged device is presented in Fig. 8(a). The as-assembled w-LED had a low CCT (3518 K) and high CRI (84.7), which indicates that it has a warm white light and meets the requirements of lighting and display applications. As shown in Fig. 8(b), the resulting w-LED exhibited the CIE chromaticity coordinates of (0.4009, 0.3833), verifying that the red emission from SLIO:Eu^{3+} is well-suited for constructing warm white lighting. The photograph of the operating device (inset of Fig. 8(b)) further confirmed bright and visually uniform light output. The radar chart revealed that the CRI factors were much higher than commercial w-LEDs, especially filling the drawbacks in the red range (R9 rose from 30 to 67), enhancing color fidelity compared to conventional commercial w-LEDs.[66] Such high CRI values reflect the device's strong capability to reproduce natural colors with high accuracy under illumination. To examine the electrical reliability of the phosphor under practical driving conditions, EL spectra were recorded over a current range of 50–300 mA (Fig. 8(d)). With increasing drive current, the emission intensity increased proportionally, while the spectral shape and peak positions remained nearly unchanged, showing no discernible spectral distortion or wavelength shift. This strongly demonstrates the outstanding electrical and spectral stability of SLIO:Eu^{3+}, even under high current injection. Notably, these results indicate that SLIO:Eu^{3+} phosphors possess excellent luminescence performance, superior color quality, and robust operational stability, making them a promising candidate for NUV-excited w-LED applications. Its ability to maintain color fidelity and emission intensity under elevated electrical load further highlights its great potential for next-generation solid-state lighting, particularly in high-power, high-CRI, and warm white illumination systems.

4. Conclusion

In summary, a new red-emitting phosphor $SrLaInO_4$:Eu^{3+} (SLIO:Eu^{3+}) was developed and evaluated for NUV-driven warm w-LED applications. Structural characterization confirmed that the Eu^{3+} ions were preferentially accommodated into the non-centrosymmetric La^{3+} sites, effectively activating the hypersensitive $^5D_0 \rightarrow {}^7F_2$ transition and producing spectrally narrow red emission. In addition, the band gap narrowing induced by Eu^{3+} incorporation contributes to enhanced absorption in the NUV region. The optimal concentration of Eu^{3+} ions in the SLIO host was determined as x = 0.2 mol, and outstanding luminescence performance was observed, including a high color purity of 95%. Concentration quenching was analyzed to originate from electric dipole–dipole interactions, while J–O analysis revealed a large Ω_2/Ω_4 ratio, further confirming the highly asymmetric local environment surrounding Eu^{3+}. A warm w-LED device integrating SLIO:Eu^{3+} demonstrated stable warm white light output with a high CRI and low CCT, highlighting its potential as a high-purity red component. These results suggest $SrLaInO_4$:Eu^{3+} as a potential phosphor for the design of next-generation red-emitting materials in advanced solid-state lighting and display systems.

Conflicts of interest

The authors declare that they have no known competing financial interests or personal relationships that could have appeared to influence the work reported in this paper.

Data availability

The data are available from the corresponding author on reasonable request.

Supplementary information (SI) is available. See DOI: https://doi.org/10.1039/d5qi02595h.

Acknowledgements

This work was supported by the National Research Foundation of Korea (NRF) grant funded by the Korean government (MSIT) (RS-2025-23963824).

References

1 Z. Li, H. Wang, Z. Su, R. Kang, T. Seto and Y. Wang, Enhanced Quantum Efficiency via Co-Substitution in Red-Emitting Phosphor $Sr_2[MgAl_5N_7]$:Eu^{2+} for Advanced Spectroscopic Applications Including Laser Displays with Ultra-High Luminescence Saturation Threshold, *Angew. Chem., Int. Ed.*, 2025, **64**, e202419910.
2 Y. Zhou, C. Li, F. Tang, X. Fang, X. Li, X. Lao, G. Du and S. Xu, Highly Efficient Large–Size Ultrathin Phosphor–Glass Composites for Super–Bright LED Lights, *Laser Photonics Rev.*, 2025, **20**, e01513.
3 M. Hua, S. Liu, L. Zhou, J. C. Bunzli and M. Wu, Phosphor-converted light-emitting diodes in the marine environment: current status and future trends, *Chem. Sci.*, 2025, **16**, 2089–2104.
4 Z. Jia, C. Yuan, Y. Liu, X. J. Wang, P. Sun, L. Wang, H. Jiang and J. Jiang, Strategies to approach high performance in Cr^{3+}-doped phosphors for high-power NIR-LED light sources, *Light:Sci. Appl.*, 2020, **9**, 86.
5 X. Chen and X. Huang, Full-Visible-Spectrum White LEDs Enabled by a Blue-Light-Excitable Cyan Phosphor, *ACS Appl. Mater. Interfaces*, 2024, **16**, 57365–57376.
6 P. Khajuria, V. D. Sharma, A. Khajuria, R. Prakash and R. J. Choudhary, Synthesis and Spectroscopic Investigations of Sm^{3+} Activated ZrO_2 and Na_2ZrO_3 as Warm Light Phosphors, *J. Fluoresc.*, 2025, **35**, 2023–2038.
7 C. Chen, R. Chen, R. Gao, J. Zheng, J. Xiang and C. Guo, Highly Efficient and Stable Narrow Band Green Emitting

Phosphor of Sb^{3+}/Ce^{3+} Sensitized $Cs_2NaTbCl_6$ for WLED, *Laser Photonics Rev.*, 2024, **19**, 201158.

8 R. Zhou, D. Hua, B. Liu, M. Guo, Q. Li, J. Li, T. Deng and J. Zhou, RGB-tricolor multimodal luminescence of Ce^{3+} and Mn^{2+} in $Mg_2Al_4Si_5O_{18}$ via site occupancy engineering for anticounterfeiting applications, *Mater. Today Chem.*, 2024, **40**, 102287.

9 S. Zhu, S. Jin, T. Pang, L. Zeng, L. Lei, F. You, Y. Fang and D. Chen, Local structure engineering of $Ba_{1(-x}K_xLa_2Y_2(SiO_4)_2O_{1-\alpha}$: Eu^{2+} green phosphors for violet-light-excitable full-spectrum lighting, *J. Alloys Compd.*, 2024, **1007**, 176407.

10 W. Xiang and J. S. Yu, Synthesis and photoluminescence properties of high-quality reddish-orange emitting $Ca_4Nb_2O_9:Eu^{3+}$ phosphors for WLEDs and anti-counterfeiting, *Dalton Trans.*, 2024, **53**, 10178–10188.

11 T. Zheng, M. Runowski, J. Xue, L. Luo, U. R. Rodríguez-Mendoza, V. Lavín, I. R. Martín, P. Rodríguez-Hernández, A. Muñoz and P. Du, Giant Pressure–Induced Spectral Shift in Cyan–Emitting Eu2+–Activated Sr8Si4O12Cl8 Microspheres for Ultrasensitive Visual Manometry, *Adv. Funct. Mater.*, 2023, **33**, 2214663.

12 W. Xiang and J. S. Yu, Preparation and photoluminescence performances of orange-red-emitting Sm^{3+}-doped $BaIn_2(P_2O_7)_2$ phosphors for flexible display and anti-counterfeiting, *Ceram. Int.*, 2025, **51**, 24297–24305.

13 X. Peng, S. Li, Z. Liu, B. Zhang, Y. Peng, D. Yu, R. Tian, X. Yao, Z. Huang, X. Liu and R.-J. Xie, Highly thermal conductive red-emitting AlN-$CaAlSiN_3:Eu^{2+}$ composite phosphor ceramics for high-power laser-driven lighting, *J. Eur. Ceram. Soc.*, 2021, **41**, 5650–5657.

14 J. Li, Z. Long, X. Jiang, J. Yang, D. Zhou, Y. Yang, Q. Wang, H. Wu and J. Qiu, Enhancement of the dynamic luminescence and self-recovery performance of Zn^{2+} co-doped $Sr_3Ga_4O_9:Sm^{3+}$, *Inorg. Chem. Front.*, 2024, **11**, 8762–8769.

15 Y. Hua, W.-X. Yang and W. Ran, Garnet-structure phosphors with ultra-high color purity red emission for potential warm WLED and flexible-transparent displays, *Ceram. Int.*, 2024, **50**, 50516–50525.

16 W. Chen, Site occupancy and tunable luminescence of Eu^{2+} and Eu^{3+} coactivated $KCaY(PO_4)_2$:Eu phosphors, *Luminescence*, 2024, **39**, e4809.

17 R. Kameshwaran, A. Raja, R. R. Kumar, D. J. Daniel, D. O. Annalakshmi, K. Aravinth, P. B. Bhargav and P. Ramasamy, Synthesis, structure and luminescence properties of bifunctional $KCaF_3$ phosphor influenced by incorporating Eu^{3+} ions for solid state lighting and TL dosimetry applications, *Appl. Radiat. Isot.*, 2023, **191**, 110520.

18 J. Qiang, L. Hou, L. Wang, Y. Li, H. Ruan, J. Li, S. Liao and Y. Huang, Boosting the red emission and luminescent thermostability of $GdPO_4:Eu^{3+}$ phosphors by coating with graphitic carbon nitride, *J. Lumin.*, 2024, **273**, 120652.

19 C. H. Hsu, C. E. Liu, L. Y. Lai, M. T. Kuo, J. R. He and H. P. Lin, Synthesis of Mesoporous Eu^{3+}-Doped Zinc/Silicate Phosphors for Highly Selective and Sensitive Detection of Sulfide Ions, *ACS Omega*, 2023, **8**, 44229–44237.

20 Y. Chen, H. Zhang, K. Liu, X. Zhu and H. Yuan, Luminescence performance of $CaYGaO_4:Bi^{3+}$, $CaYGaO_4:Mn^{4+}$ and $CaYGaO_4:Bi^{3+}/Mn^{4+}$ phosphors, *J. Alloys Compd.*, 2022, **918**, 165759.

21 S. Liu, S. Gao, D. Gao, L. Wang, W. Song, H. Yin, Y. Zhu, J. Zhang, Q. Yu and X. Chen, Up-conversion phosphor $LaCaGaO_4$: Er^{3+}/Yb^{3+} for the optical temperature sensing and anti-counterfeiting, *Curr. Appl. Phys.*, 2025, **73**, 84–97.

22 Y. Zhao, Z. Li, J. Wang, X. Zhao, C. Liu, J. Ban, X. Zhang, H. Zhou and X. Jiang, Enhanced photoluminescence of a novel red-emitting phosphor of $CaLaGaO_4:Eu^{3+}$ by lithium ion doping, *Opt. Mater.*, 2025, **167**, 117229.

23 Y. Qiu, R. Cui, M. Zhang and C. Deng, Dual-emitting Dy^{3+}/Eu^{3+} co-doped $SrLaGaO_4$ phosphor: Tunable luminescence, energy transfer and ratiometric temperature sensing, *J. Mol. Struct.*, 2024, **1304**, 137622.

24 X. Peng, X. Guo, R. Cui, P. Ling-hu, J. Zhang and C. Deng, Novel orange red phosphor $BaLaGaO_4$: Sm^{3+} with high quantum efficiency and good thermal stability for indoor illumination and anti-counterfeiting inks applications, *Ceram. Int.*, 2024, **50**, 30111–30123.

25 S. Gai, P. Gao, K. Chen, C. Tang, Y. Zhao, J. Wei, Y. Zhang, M. S. Molokeev, M. Xia and Z. Zhou, Superior Quantum Efficiency Blue–Emitting Phosphors with High Thermal Stability toward Multipurpose LED Applications, *Adv. Opt. Mater.*, 2024, **12**, 2302870.

26 C. R. Garcia, J. Oliva, J. Carranza, A. I. Mtz-Enriquez, H. M. Hdz-Garcia, A. Santibañez and D. Chavez, Green Upconversion of a $SrLaAlO_4$:Yb,Er Phosphor and Its Application for LED Illumination, *J. Electron. Mater.*, 2023, **52**, 1357–1365.

27 A. Martinović, B. Milićević, J. Periša, Z. Ristić, S. Stojadinović, M. D. Dramićanin and A. Ćirić, Thermometric Judd-Ofelt model for Dy^{3+} ion tested in $CaYAlO_4$ host and evaluation of its sensing performances for luminescence thermometry, *Phys. B*, 2023, **666**, 415096.

28 Y. Xie, M. Gu, M. Chen, L. Cao, S. Zhang, Y. Wang, F. Niu and H. Yan, Layered Fe-doped $SrLaInO_4$ perovskite electron transport layer for dye-sensitized solar cell with high open-circuit voltage, *Mater. Lett.*, 2023, **349**, 134809.

29 N. Tarasova, A. Galisheva and I. Animitsa, Spectroscopic and transport properties of Ba– and Ti–doped $BaLaInO_4$, *J. Raman Spectrosc.*, 2021, **52**, 980–987.

30 B.-M. Liu, W.-J. Gan, S.-Q. Lou, R. Zou, Q. Tang, C.-X. Wang, J. Jiao and J. Wang, X-ray-activated, UVA persistent luminescent materials based on Bi-doped $SrLaAlO_4$ for deep-Seated photodynamic activation, *J. Appl. Phys.*, 2021, **129**, 120901.

31 P. Linghu, X. Gong, J. Zhang, R. Cui and X. Guo, A novel red $BaLaInO_4$: Eu^{3+} phosphor for WLEDs, *J. Solid State Chem.*, 2023, **327**, 124282.

32 P. Ling-Hu, X. Guo, J. Hu, C. Deng and R. Cui, Anomalous $^5D_0 \rightarrow {}^7F_4$ Transition of Eu^{3+}–Doped $BaLaGaO_4$ Phosphors for WLEDs and Plant Growth Applications, *Adv. Opt. Mater.*, 2023, **12**, 2301760.

33 Y. Qiu, R. Cui, J. Zhang and C. Deng, A novel Eu^{3+}-doped $SrLaGaO_4$ red phosphor with high efficiency and color purity for WLED applications, *J. Solid State Chem.*, 2023, **327**, 124265.

34 M. Yan, C. Yue, Y. Pu, D. Zhu and Q. Yan, Fluorescence and crystal structure of $SrLa_{1(-x}AlO_4$:xEu^{3+} phosphor synthesized using a sol-gel method, *Luminescence*, 2021, **36**, 1775–1780.

35 A. Ćirić, S. Stojadinović, M. Sekulić and M. D. Dramićanin, JOES: An application software for Judd-Ofelt analysis from Eu^{3+} emission spectra, *J. Lumin.*, 2019, **205**, 351–356.

36 B. H. Toby and R. B. Von Dreele, GSAS-II : the genesis of a modern open-source all purpose crystallography software package, *J. Appl. Crystallogr.*, 2013, **46**, 544–549.

37 L. Troncoso, J. A. Alonso and A. Aguadero, Low activation energies for interstitial oxygen conduction in the layered perovskites $La_{1+x}Sr_{1-x}InO_{4+\delta}$, *J. Mater. Chem. A*, 2015, **3**, 17797–17803.

38 Y. Kitagawa, J. Ueda and S. Tanabe, A brief review of characteristic luminescence properties of Eu^{3+} in mixed-anion compounds, *Dalton Trans.*, 2024, **53**, 8069–8092.

39 Y. Wu, Y. Li, C. Zhou, H. Chen, S.-W. Cheong, Y. Li, X. Tao and L. Zhang, Novel Geometric Ferroelectric $EuInO_3$ Single Crystals with Topological Vortex Domains, *Cryst. Growth Des.*, 2023, **23**, 1980–1986.

40 Y. Yang, Z. Lu, H. Fan, M. Chen, L. Shen, X. Zhang, Q. Pang, J. Chen, P. Chen and L. Zhou, Ultra-Broadband Near-Infrared Phosphors Realized by the Heterovalent Substitution Strategy, *Inorg. Chem.*, 2023, **62**, 3601–3608.

41 S. Tang, Q. Yuan, J. Wang, T. Wang, W. Xiang, J. Li and J. S. Yu, From 2D to 3D: WS_2/MoS_2 heterostructure *in situ* anchored on $Ti_3C_2T_x$ MXene with enhanced ion/electron migration and sodium storage at −20 °C, *Energy Storage Mater.*, 2024, **68**, 103357.

42 S. Sreevalsa, P. A. Parvathy, S. K. Sahoo and S. Das, Full-color emitting crystal engineered $Sr_3Al_{1-x}Si_xO_{4+x}F_{1-x}$:$Eu^{2+/3+}$ oxyfluorides for developing bendable lighting composites, *J. Alloys Compd.*, 2021, **880**, 160483.

43 D. Kubba, I. Ahmed, A. Roy, P. Kour, C. S. Yadav, S. K. Sharma, K. Yadav and K. K. Haldar, $LaFe_{1-x}Co_xO_3$ Perovskite Nanoparticles Supported on $Ni(OH)_2$ as Electrocatalyst for the Oxygen Evolution Reaction, *ACS Appl. Nano Mater.*, 2024, **7**, 1536–1547.

44 J. Li, Y. Sheng, G. Tong, H. Zhu, X. Tao, C. Wu, Y. Chang, Z. Tang, J. Yang, S. Zhang and Y. Jiang, Anti–Solvent Synthesis of Three–Color Indium–Based Halide Perovskite Microplate/Microcrystal Phosphors for High Color Rendering WLEDs, *Adv. Opt. Mater.*, 2023, **11**, 2300100.

45 F. Wang, H. Chen, S. Zhang, S. Zhang and H. Jin, Energy transfer of Eu^{2+}→Eu^{3+} improves the photoluminescence properties of orange-red phosphor La_2O_2S:Eu, *J. Alloys Compd.*, 2023, **969**, 172394.

46 W. Xiang and J. S. Yu, Multi-channel lifetime thermometry and security films based on Ln (Ln = Sm^{3+}, Tb^{3+}, and Sm^{3+}/Tb^{3+}) doped $NaKLaNbO_5$ phosphors, *Opt. Laser Technol.*, 2025, **180**, 111450.

47 R. K. Tamrakar, D. P. Bisen and N. Brahme, Comparison of photoluminescence properties of Gd_2O_3 phosphor synthesized by combustion and solid state reaction method, *J. Radiat. Res. Appl. Sci.*, 2014, **7**, 550–559.

48 M. Ilhan, L. F. Guleryuz and M. I. Kati, Exploring the effect of boron on the grain morphology change and spectral properties of Eu^{3+} activated barium tantalate phosphor, *RSC Adv.*, 2024, **14**, 2687–2696.

49 M. İlhan and L. F. Güleryüz, A study on the structural, morphological, spectral properties of $BaTa_2O_6$:RE^{3+}, B^{3+} (RE = Sm, Dy) phosphors and the comparison of asymmetry ratios based on the hypersensitive transition of $BaTa_2O_6$:Eu^{3+}, B^{3+} phosphor, *J. Mater. Sci.: Mater. Electron.*, 2024, **36**, 71.

50 H. Fei, B. Jing, J. Han, K. Shan, D. Cheng, X. Xu, X. Zhang and J. Wang, Crystal structure, Bi^{3+} yellow luminescence, and high quantum efficiency of $Ba_3SbAl_3Ge_2O_{14}$:Bi^{3+} phosphor for white light-emitting diodes, *Inorg. Chem. Front.*, 2024, **11**, 2616–2625.

51 Y. Zhou, Q. Cao, Y. Han, Z. Qiu, J. Zhang, W. Zhou and S. Lian, Achieving a Cr^{6+}-free Cr^{3+}-activated spinel phosphor by a one-step solid-state reaction, *Inorg. Chem. Front.*, 2024, **11**, 6127–6134.

52 I. Ayoub, U. Mushtaq, G. B. Nair, G. Sundaram, H. C. Swart and V. Kumar, Exploring the $Sr_2Ga_2GeO_7$:Tb^{3+} Long Persistent Luminescence Phosphor for Cutting-Edge Forensic Solutions in Latent Fingerprint Detection and Anticounterfeiting Applications, *Small*, 2025, **21**, e2500285.

53 L. F. Güleryüz and M. İlhan, Enhancing luminescence efficiency and optical gain of Ca_2GdMO_6:Eu^{3+} (M = Nb, Ta) phosphors via B^{3+} co-doping for forensic imaging applications, *Ceram. Int.*, 2025, **51**, 63280–63295.

54 M. İlhan, L. F. Güleryüz, S. Gökçe and S. Kılıç, Judd-Ofelt and photoluminescence analysis of Ca_2GdSbO_6:Eu^{3+} and Ca_2GdSbO_6:Eu^{3+}, B^{3+} phosphors for red emission performance, *Mater. Sci. Eng., B*, 2025, **322**, 118662.

55 R. S. Perala, M. Srivastava, B. P. Singh, V. N. K. Putta, R. Acharya and R. S. Ningthoujam, Altering of the Electric and Magnetic Dipole Transition Probability of Eu^{3+} in YPO_4 Lattice by Codoping of K^+ Ion: Potential Materials for Imaging and Heating, *Ind. Eng. Chem. Res.*, 2022, **61**, 9755–9762.

56 R. Yang, J. Li, X. Xie, J. Lian, C. Wang, C. Li, H. Su, Z. Zou, S. Xie and R. Yu, Spectroscopic investigation of $K_5La(MoO_4)_4$:Sm^{3+} red phosphor with excellent thermal stability and color purity for white LEDs, *J. Lumin.*, 2024, **267**, 120366.

57 P. Rohilla, A. Prasad and A. S. Rao, Structural and luminescence studies on thermally stable Bi^{3+}–activated Ba_3MoTiO_8 phosphors for near UV–pumped w–LED applications, *Int. J. Appl. Ceram. Technol.*, 2023, **21**, 1208–1219.

58 L. Wang, Y. Zhang, D. Gao, X. Sha, X. Chen, Y. Zhang, J. Zhang, X. Zhang, Y. Cao, Y. Wang, X. Li, S. Xu, H. Yu and B. Chen, Concentration- and temperature- dependent luminescence quenching and optical transition of

Sr_2GdTaO_6: Eu^{3+} phosphor for potential applications in white LEDs, *Results Phys.*, 2024, **56**, 107238.

59 R. T. Maske, A. N. Yerpude, R. S. Wandhare, A. Nande and S. J. Dhoble, Combustion synthesized novel $SrAlBO_4$:Eu^{3+} phosphor: Structural, luminescence, and Judd-Ofelt analysis, *Opt. Mater.*, 2023, **141**, 113893.

60 A. Princy, S. M. M. Kennedy, K. J. Albert and V. R. Mala, Judd-Ofelt analysis of Sm^{3+} doped $Ca_2LiMg_2V_3O_{12}$ phosphors: Unveiling luminescent and thermometric properties for multifunctional applications, *Ceram. Int.*, 2024, **50**, 30229–30239.

61 W. T. Carnall, P. R. Fields and K. Rajnak, Electronic Energy Levels in the Trivalent Lanthanide Aquo Ions. I. Pr^{3+}, Nd^{3+}, Pm^{3+}, Sm^{3+}, Dy^{3+}, Ho^{3+}, Er^{3+}, and Tm^{3+}, *J. Chem. Phys.*, 1968, **49**, 4424–4442.

62 P. J. Chaware, Y. D. Choudhari, D. M. Borikar and K. G. Rewatkar, Photoluminescence and Judd-Ofelt analysis of Eu^{3+} doped akermanite silicate phosphors for solid state lighting, *Opt. Mater.*, 2022, **133**, 112945.

63 A. S. Altowyan, U. H. Kaynar, C. Gök, H. Aydin, J. Hakami, M. B. Coban, A. Canimoglu and N. Can, Photoluminescence characteristics and Judd-Ofelt analysis of $YBa_3(BO_3)_3$:Tb^{3+} phosphors co-doped with Li^+, Na^+, and K^+, *J. Lumin.*, 2025, **286**, 121380.

64 S. Gao, S. Liu, D. Gao, X. Chen, X. Zhang, J. Tan, L. Wang, W. Song, H. Yin and Y. Zhu, Photoluminescence properties, temperature sensing and Judd-Ofelt analysis of $Lu_2Ge_2O_7$:Eu^{3+} phosphors and the application in optical anti-counterfeiting and latent fingerprint visualization, *Ceram. Int.*, 2025, **51**, 57916–57930.

65 S. Ravi, M. Venkatakrishnan, K. Rajagopalan and T. Jagannathan, Effect of Flux Addition on the Luminescence Performance of $Ca_{0.5}Gd_{1-x}(MoO_4)_2$:x$Eu^{3+}$ Phosphor: Judd-Ofelt Investigation, *J. Electron. Mater.*, 2025, **54**, 2239–2248.

66 I. S. Pruthviraj, B. R. R. Krushna, K. Karthikeyan, S. C. Sharma, S. S. Mohapatra, K. Manjunatha, S. Y. Wu, K. N. Narasimhamurthy, F. F. Komahal and H. Nagabhushana, Thermoluminescent and photoluminescent properties of $CaGd_2ZnO_5$:Er^{3+} phosphors: Insights into dosimetry and w-LED fabrication, *J. Lumin.*, 2025, **284**, 121295.

